JASA ARTICLE

Experimental investigation of low Reynolds number rotor noise

Romain Gojon,[a] Thierry Jardin,[b] and Hélène Parisot-Dupuis
Institut Supérieur de l'Aéronautique et de l'Espace (ISAE-SUPAERO), Université de Toulouse, 31400 Toulouse, France

ABSTRACT:
In this paper, an experimental characterisation of low Reynolds number rotors is performed in an anechoic room. Two commercially available two-bladed rotors as well as four three-dimensional (3D)-printed rotors with different numbers of blades (from two to five) are tested. The latter have canonical geometry, with an NACA0012 blade section profile, extruded in the radial direction with constant chord and constant 10° pitch. The experimental setup and the 3D printing strategy are first validated using results from the literature for the commercially available rotors. For all the tested rotors, four noise characteristics are analysed: the overall sound pressure level (OASPL), the amplitude of the blade passing frequency (BPF), and the amplitude of its first harmonic and the high-frequency broadband noise. For all the rotors, an increase in all noise characteristics is observed with the rotational speed (rpm) for all directivity angles. Moreover, an interesting change of pattern is observed for the amplitudes of the BPF and of its first harmonic, with, in the vicinity of the rotor plane, a minimum value for low rpm and/or high number of blades, and a maximum value for high rpm and/or low number of blades. This change in directivity leads to a similar change of directivity of the OASPL. For the broadband noise, a dipole-like pattern is obtained with a minimum value at $\theta = -10°$, i.e., aligned with the trailing edge and thus indicating the generation of trailing edge noise. Finally, scaling laws that characterise the amplitude of the different noise components with respect to the rpm are proposed.
 https://doi.org/10.1121/10.0005068
(Received 8 October 2020; revised 6 May 2021; accepted 7 May 2021; published online 3 June 2021)
[Editor: D. Keith Wilson] Pages: 3813–3829

I. INTRODUCTION

In the near future, intra-city transportation may well be revolutionized by urban air mobility (UAM), i.e., new technologies of vertical takeoff and landing (VTOL) manned and unmanned aerial vehicles (UAVs). UAM technologies are actively being considered by industry and research laboratories as a means to conduct operations in the low-altitude urban airspace, including rescue operations, transport of blood and organs between hospitals, medical evacuations, passenger transport, traffic monitoring, and package delivery, to name a few. However, with the development of UAVs and the potential increase in urban air traffic, many questions arise regarding how this new paradigm may be perceived by the civilian population in terms of safety, privacy violations, and visual and auditory disturbances. To cope with this situation, agencies like the Federal Aviation Administration (FAA) and European Union Aviation Safety Agency (EASA) may soon put in place more stringent certification standards. However, defining relevant certification standards, and then designing vehicles that comply with these standards, requires deeper insight into robustness, reliability, safety, ethics, aeroacoustical sciences, etc.

The specific question of noise pollution mostly relies on the use of rotors for VTOL capabilities. The evaluation and prediction of rotor noise in itself is not new (e.g., George, 1978; Brentner and Farassat, 1994), but most studies conducted on this topic in recent decades are mainly concerned with helicopters. While helicopters operate at high Reynolds numbers and relatively high Mach numbers (say within the transonic regime) and generally feature one rotor, UAVs may operate at much lower Reynolds and Mach numbers and may feature complex interactions between multiple rotors. Hence, extensive knowledge on helicopter noise may not be directly transposable to all UAM technologies.

The aeroacoustics of low Reynolds number and low Mach number rotors have only recently been addressed. Zawodny *et al.* (2016) reported experiments on small-scale (diameters of 9.4 and 11 in.) rotors operating under hovering conditions. They showed that the far-field spectrum is characterized by tonal noise at the blade passing frequency (BPF) and harmonics and broadband noise at mid and high frequency. Tonal noise from the brushless motor was also observed, which was partly correlated with its number of magnetic poles and the rotation frequency. The authors also reported numerical data from low-fidelity (blade element analysis) and high-fidelity [unsteady Reynolds-averaged Navier–Stokes (URANS)] simulations coupled with a Ffowcs Williams–Hawkings (FW-H) approach and broadband models. Tonal noise from the rotor was found to be reasonably well predicted by both approaches. Jo *et al.* (2019) used a non-linear vortex lattice method (NL-VLM) coupled with a FW-H analysis to study the effect of the

[a]Electronic mail: romain.gojon@isae-supaero.fr, ORCID: 0000-0003-4543-338X.
[b]ORCID: 0000-0001-9704-2984.

number of blades on the aeroacoustics of hovering rotors. They found that, for a given target thrust, rotor performance was enhanced for a number of blades of 3 and that, despite the increasing influence of blade-vortex interactions, acoustic noise monotonically decreased with the number of blades. Serré *et al.* (2019a) and Serré *et al.* (2019b) performed an aeroacoustic optimization of a hovering rotor through low-order models (blade element, FW-H, and broadband models). They showed that the overall rotor noise could be significantly reduced as compared with conventional off-the-shelf rotors. Further investigations using high-fidelity simulations [large eddy simulation (LES)] suggested that, apart from tonal noise at the BPF, a dominant source of noise arose from interactions of the wake with the blade leading edge, whereas trailing edge noise was of secondary importance. In that regard, the authors suggested that wavy leading edges could further reduce noise generation.

In addition to isolated rotors, a few studies reported results on rotor-frame and rotor-rotor interactions. Zawodny and Boyd (2017) investigated rotor-frame interaction noise in simplified configurations representative of hovering rotors, through both experiments and numerical simulations. The authors showed that rotor-frame interactions produce additional noise that is, however, highly dependent on frame geometry, position of the frame with respect to the rotor disk plane (below or above), and distance to the rotor disk plane. More complex configurations with multiple rotors and airframes were investigated by Intaratep *et al.* (2016), Tinney and Sirohi (2018), and Yoon *et al.* (2017), among others. However, although the analysis of complex configurations may lead to the identification of prominent aeroacoustic sources, to leading order, it is not very well suited to the fundamental understanding of the precise physical phenomena underlying noise generation, which is ultimately required to develop efficient low-order models.

In this paper, we report on an experimental investigation of the noise generated by a small-scale isolated rotor operating under hovering conditions. The characteristic Reynolds number is here in the range of 2×10^4 to 2×10^5, i.e., typical of small UAVs. In this range, peculiar aerodynamic phenomena (e.g., laminar-to-turbulent transition, laminar separation bubble) may occur and subsequently affect the aeroacoustic footprint. This is a fundamental difference from higher Reynolds number configurations typical of helicopters and may lead to a relatively high sensitivity of rotor aerodynamics and aeroacoustics to the rotational speed. The aim of the present work is principally threefold.

First, as a complement to previous experiments by Zawodny *et al.* (2016), we wish to provide the community with an experimental database that may serve as a benchmark for the assessment of numerical approaches. In that sense, (i) we used an industrial brushless motor with low noise emission, rather than conventional off-the-shelf, brushless motors, to better isolate rotor noise; (ii) we ensured that our rotors were not subjected to airflow recirculation within the anechoic room, which tends to overestimate noise, as recently highlighted by Stephenson *et al.* (2019); and (iii) we used manufactured in-laboratory, three-dimensional (3D)-printed rotors whose geometry is known. In addition, we evaluate the influence of the blowing direction and the manufacturing process and perform repeatability tests over different specimens of the same rotor. All the results are available as an open database for the UAV acoustic community to help draw general guidelines for the design of low noise rotors (ISAE-SUPAERO, 2021).

Second, we focus on the noise generated by three different two-bladed rotors. We analyse far-field spectra and derive directivity plots for a range of rotational speeds from 2000 to 9000 rpm to provide insight into the different tonal and broadband noise components. In addition, we derive scaling laws that characterise the amplitude of the different noise components with respect to the rpm.

Finally, we evaluate the influence of the number of blades on both aerodynamic and aeroacoustic performance. As for two-bladed rotors, we demonstrate changes in directivity plots with increasing rpm and show that scaling laws derived for two-bladed rotors generally apply to rotors with more than two blades.

II. EXPERIMENTAL SETUP

The experimental setup consists of an isolated rotor placed at the center of ISAE-SUPAERO anechoic room (see Fig. 1). This facility is acoustically treated in the frequency range 80–16 000 Hz and has wedge-tip to wedge-tip dimensions of 5.02 m long, 5.24 m wide, and 5.34 m high.

The rotor is positioned at the center of the anechoic room at the top of a rotor test stand and is driven by means

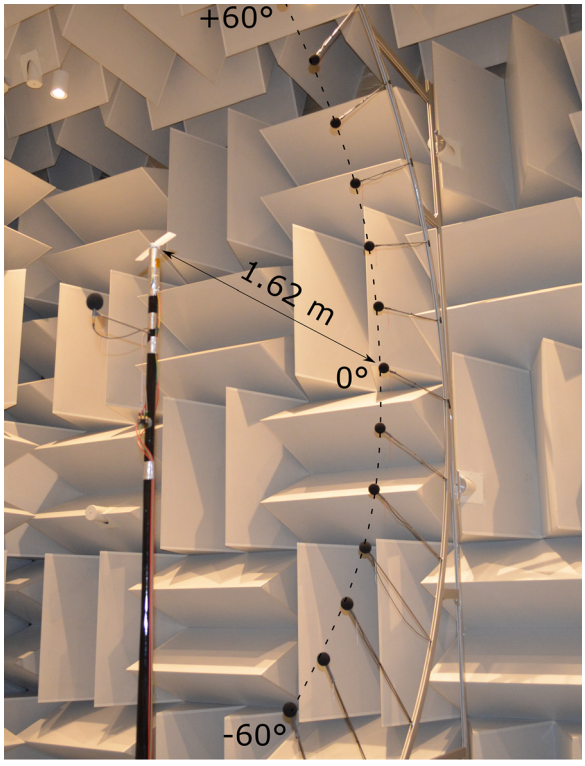

FIG. 1. (Color online) Photograph of the experimental setup.

https://doi.org/10.1121/10.0005068

of a Faulhaber (Schönaich, Germany) 3274G024BP4 3692 electric brushless motor, which has low noise emissions as compared to conventional off-the-shelf motors. Real time rpm are directly given by the associated motion controller MC5010, which provides a precise speed control.

A six-axis ATI (Apex, NC) Nano17 load cell is placed beneath the motor for measuring aerodynamic loads. Note that only two components are of interest here, namely rotor thrust T (N) and torque Q (N·m). In what follows, time-averaged thrust and torque are presented under their non-dimensional form $C_T = T/(\rho f^2 D^4)$ and $C_Q = Q/(\rho f^2 D^5)$, respectively. Here, ρ, f, and D are the fluid density, rotor rotational frequency, and rotor diameter, respectively. Note that ρ is computed from the ideal gas law with the pressure and temperature in the anechoic room. Time signals of T and Q (and other variables like rpm, pressure, and temperature) are acquired at a frequency of 2 kHz during 16 s after initial transients have decayed (i.e., typically 30 s after the rpm was changed). Time-averaging is performed over the whole 16 s time window, which ensures statistical convergence.

In addition, a three-axis accelerometer A/34 from DJB Instruments (Mildenhall, UK) is placed 0.25 m below the rotor plane to monitor potential vibrations of the rotor test stand, as induced by rotor rotation.

A directivity antenna with 13 1/4 in. GRAS (Holte, Denmark) 40PH microphones is used to measure the far-field noise 1.62 m away from the rotor center, every 10° from −60° to 60°, where 0° corresponds to the rotor disk plane. Moreover, a near-field microphone is placed 0.25 m below the rotor disk plane and 0.25 m away from the rotor center, in the radial direction. Acoustic data are acquired at a sampling frequency of 51.2 kHz during 16 s. Acoustic narrowband spectra are obtained from time signals by computing the fast Fourier transform (FFT) with a Hanning window applied on 50 segments, using a 50% overlap and an amplitude correction factor. The frequency resolution is $\Delta f = 3.125$ Hz. To quantify the random sound pressure level (SPL) uncertainty, we follow the work of Zawodny and Boyd (2017). Considering that 50 segments and a Hanning window whose mean value is 0.5 are used, an autospectral random uncertainty of 10% can be found (Bendat and Piersol, 2010). This autospectral random uncertainty leads to a random SPL uncertainty of (–0.45, +0.41) dB.

Several rotors are considered, including commercially available two-bladed APC 9 × 6 SF and APC 11 × 4.7 SF rotors, as well as 3D-printed rotors with different numbers of blades (from two to five). The latter have an NACA0012 blade section profile, extruded in the radial direction with constant chord and constant 10° pitch. The stereolithography 3D printer "Form 2" was used for 3D-printing along with two photopolymer resins: the standard "Grey Pro" gray resin and the glass reinforced "Rigid" white resin. Rotor characteristics are summarized in Table I.

Because 3D-printed rotors are less robust to rotational forces than conventional off-the-shelf rotors and may break at high rpm, which may damage the ATI Nano-17 balance, the latter were only used for APC rotors. A second test bench was used to measure aerodynamic loads on the 3D-printed rotors. This pendulum type test bench consists of two 10 N S100 load cells from Strain Measurement Devices (SMD) (Wallingford, CT) for thrust and torque measurements, as shown in Fig. 2 [see also Désert (2019) and Désert *et al.* (2019)]. It is placed outside of the anechoic room; hence, load measurements were not performed simultaneously to acoustic measurements for 3D-printed rotors. Data acquisition parameters are the same as those used for APC rotors with the ATI Nano17 load cell. In what follows, data obtained from the ATI Nano 17 load cell will be flagged with #1, while data obtained from SMD load cells will be flagged with #2.

The experimental test matrix is presented in Table II.

III. ASSESSMENT OF THE EXPERIMENTAL SETUP

A. Comparison with existing data

The APC 11 × 4.7 SF rotor is used to assess our measurements with data from Brandt *et al.* (2020) and Zawodny *et al.* (2016). The database provided in Brandt *et al.* is considered as a reference in the low Reynolds number propeller/rotor community. That in Zawodny *et al.* (2016) is used, as it further includes acoustic data.

Figure 3 shows the thrust and torque coefficients obtained with the ATI Nano 17 sensor (data #1) for rotational speeds ranging from 2000 to 6000 rpm. Linear fits based on Brandt *et al.* (2020) data are added and depicted as plain black lines, together with grayed regions corresponding to ±5% of the fitted values. Overall, it can be seen that the present data agree with data from Brandt *et al.* (2020) and Zawodny *et al.* (2016) within reasonable accuracy. Although we observe consistency in the different sets of data, it is important to mention that non-negligible differences may be observed between different specimens of the same commercial rotor model, as highlighted by Deters *et al.* (2014) and in the next paragraph. In that sense, ±5% corresponds to the maximum discrepancies that we measure

TABLE I. Characteristics of the rotors.

Name	Diameter (m)	N blades	Profile	Chord length (m)	Pitch
APC 9 × 6 SF	0.23	2	Eppler E63/Clark-Y[a]	Varying	Varying
APC 11 × 4.7 SF	0.28	2	Eppler E63/Clark-Y[a]	Varying[b]	Varying[b]
ISAE 2–5	0.25	2–5	NACA0012	0.025, constant	10°, constant

[a]From APC (2021).
[b]See Zawodny *et al.* (2016) for twist and chord laws.

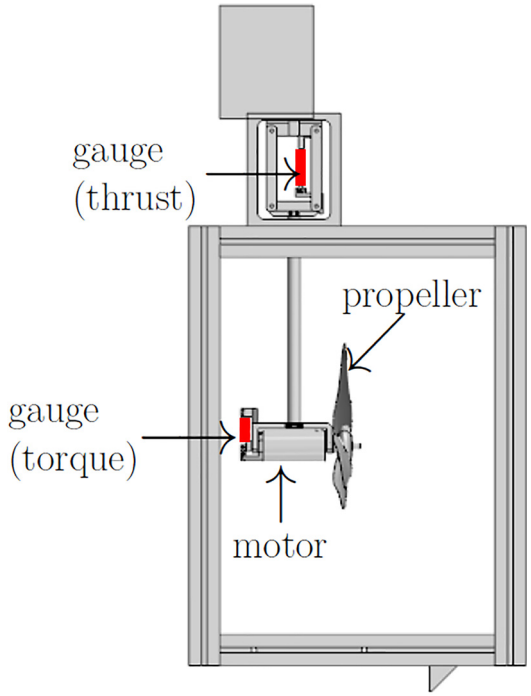

FIG. 2. (Color online) Sketch of the experimental test bench for load measurements on 3D-printed rotors.

between thrust coefficients obtained from different specimens and setups (see next paragraph), which is significantly larger than the uncertainties of the load cell (in that case, below 0.7% and 0.07% of C_T at 2000 and 6000 rpm, respectively). We also note from Fig. 3 that aerodynamic performance is largely dependent on Reynolds number (i.e., Reynolds number effects are strong), with a significant increase in both C_T and C_Q with Reynolds number. This suggests that the flow, and hence aeroacoustics, is highly sensitive to the rpm, as expected in this low Reynolds number flow regime.

Figure 4 compares the thrust and torque coefficients obtained from SMD load cells (data #2) with those obtained from the ATI Nano 17 sensor (data #1) for two specimens (A and B) of the APC 11×4.7 SF rotor. Here, again, linear fits based on data from setup #1, specimen A (previously shown in Fig. 3), are added and depicted as plain black lines, together with grayed regions corresponding to an arbitrary $\pm 5\%$ of the fitted values. It is shown that data obtained from both setups, with the same specimen, agree within reasonable accuracy. On the other hand, as previously mentioned, slight discrepancies exist between data obtained from the same setup but with two different specimens of the commercial rotor. Care should thus be taken when quantitatively comparing data from distinct experiments. However, and

TABLE II. Experimental test matrix. N/A, not applicable.

Rotors	rpm	Additional rpm	Load cells
APC	[2000:1000:7000]	[3600;4200;4800]	ATI and SMD
ISAE	[2000:500:9000]	N/A	SMD

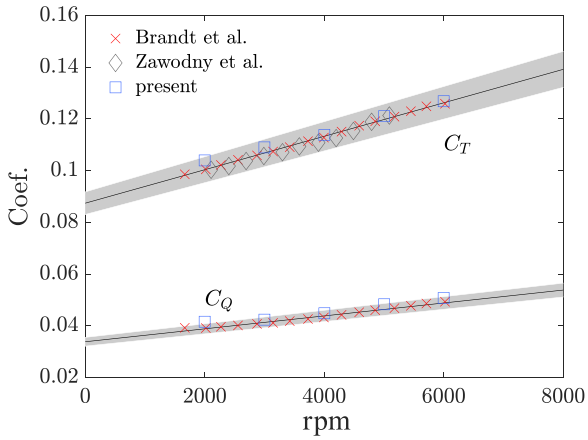

FIG. 3. (Color online) Time-averaged thrust C_T and torque C_Q coefficients as a function of rpm, obtained for the APC 11×4.7 SF rotor. Comparison between present data and those reported in Brandt *et al.* (2020) and Zawodny *et al.* (2016).

more importantly, all cases show similar trends in terms of Reynolds number effects on aerodynamic performance.

Figure 5 shows the SPLs obtained from pressure signals of the directivity antenna. Data are compared with those reported in Zawodny *et al.* (2016) for three operating conditions: 3600, 4200, and 4800 rpm. We stress that in Zawodny *et al.* (2016), microphones were located at a radial distance of 1.905 m from the rotor center, whereas they were 1.62 m away from the rotor center in our case. A scaling, assuming spherical wave propagation in free field, is thus applied to our data to allow the comparison with Zawodny *et al.* (2016) data. Two directions of blowing have been tested (i.e., toward and away from the test stand; details are provided in Sec. III B). Data presented hereafter correspond to downward blowing (i.e., toward the test stand) to be consistent with the Zawodny *et al.* (2016) setup. Also, note that the 45° elevation angle microphone used in Zawodny *et al.* (2016) was not available in our directivity antenna. Results from microphones situated 40° and 50° above the rotor plane are used instead for the comparison.

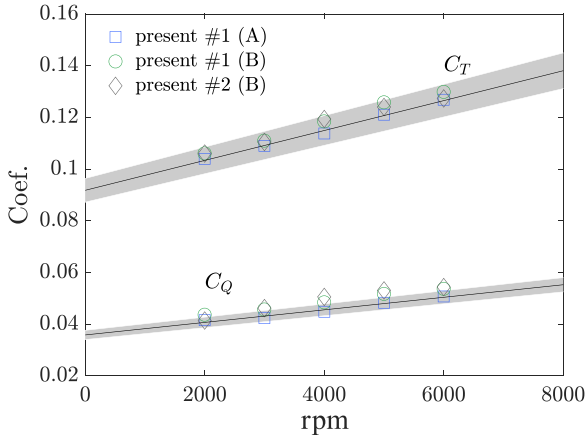

FIG. 4. (Color online) Time-averaged thrust C_T and torque C_Q coefficients as a function of rpm, obtained for the APC 11×4.7 SF rotor. Comparison between data obtained from setup #1 and #2 for two specimens (A and B).

https://doi.org/10.1121/10.0005068

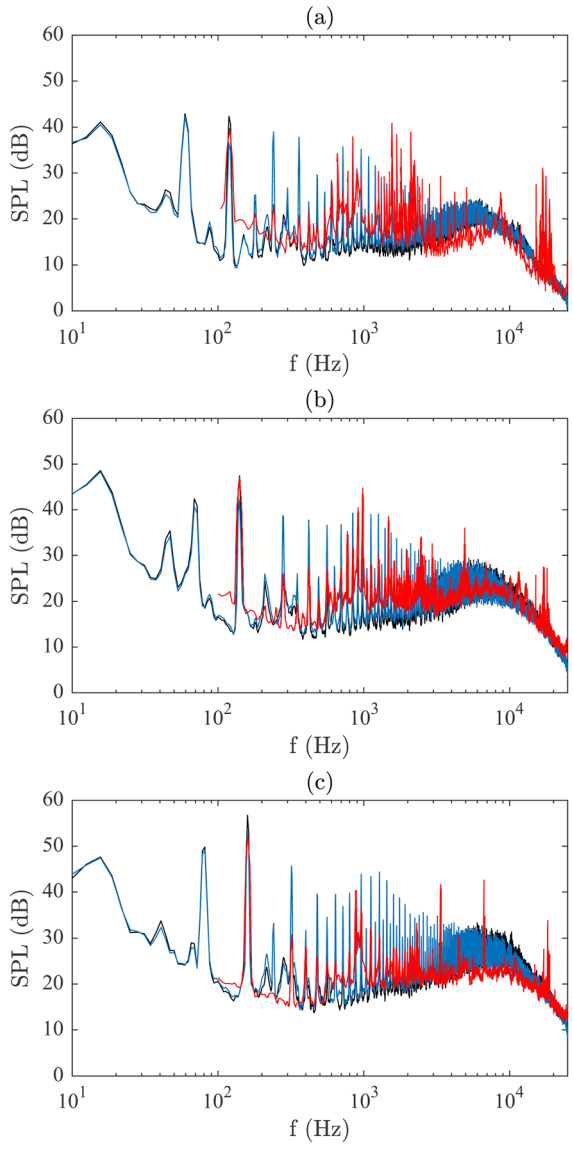

FIG. 5. (Color online) SPL at 1.905 m for the rotor APC 11 × 4.7 SF at (a) 3600, (b) 4200, and (c) 4800 rpm. Present results at angles (black line) 40° and (blue line) 50° from the rotor plane in the flow direction, and (red line) experimental results of Zawodny *et al.* (2016) at angle 45°. Rotor blowing in the downward direction.

It can be observed that the results compare reasonably well. First, for the main tone frequency due to the BPF, the amplitude found in Zawodny *et al.* (2016) is always located between the amplitude found in the present experiment at angles of 40° and 50° from the rotor plane in the flow direction, as expected. Second, large differences can be seen with several tonal frequencies measured by Zawodny *et al.* (2016) in the frequency range 500–5000 Hz. The latter were found to arise from the motor used in the authors' work (some of which are directly related to the number of poles of the motor), which differs from the "low noise" motor used in the present study. Finally, for the high- and mid-frequency broadband noises due to blade wake interaction and trailing edge noises, the results exhibit similar trends. To have a more quantitative comparison between our results and experimental results of Zawodny *et al.* (2016), the amplitudes of the main tonal noise at angles of 40° and 50° from the rotor plane in the flow direction are averaged. Results are given in Table III. Differences up to 2.8 dB can be noticed.

TABLE III. Comparison of the amplitude of the BPF tonal noise at an angle of 45° from the rotor plane in the flow direction with experimental results from the literature (Zawodny *et al.*, 2016).

rpm	BPF (dB) (40° and 50° averaged)	BPF (dB) (Zawodny *et al.*, 2016)
3600	39.5	39.7
4200	44.8	47.0
4800	55.3	52.5

B. Blowing direction

In this section, we highlight the influence of the blowing direction on both aerodynamic loads and far-field acoustics. We consider the APC 11 × 4.7 SF rotor either blowing in the downward direction, toward the test stand, or blowing in the upward direction, away from the test stand.

Figure 6 depicts the thrust and torque coefficients obtained for both cases. Linear fits of data obtained with the rotor blowing in the upward direction are also shown. While there is no clear difference between torque coefficients, some differences are observed on thrust coefficients, with slightly larger levels for the rotor blowing in the downward direction. However, these differences are not significant here and are within the range of values obtained with different setups and different specimens of the same rotor (see Sec. III A). Again, the overall trend with respect to Reynolds number is unaffected.

Figure 7 shows the SPL obtained from pressure signals at the far field, in the rotor disk plane, for two different rpm. Note that for the case at 5000 rpm, a repetition of each measurement is also plotted to emphasize the repeatability of the measurement.

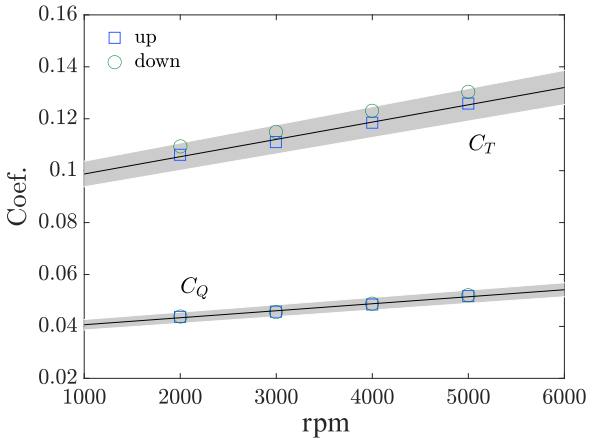

FIG. 6. (Color online) Time-averaged thrust C_T and torque C_Q coefficients as a function of rotor rpm, obtained for the APC 11 × 4.7 SF rotor. Comparison between data obtained from setup #1 with the rotor blowing in the upward and downward directions.

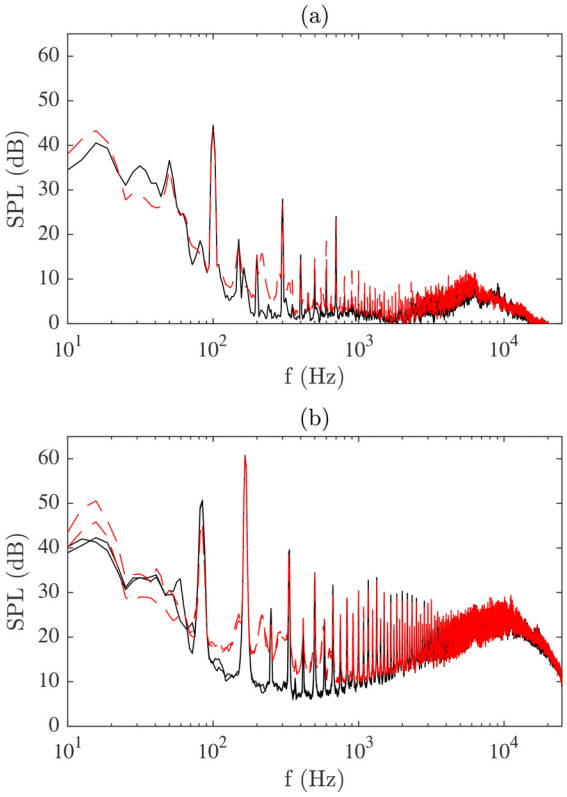

FIG. 7. (Color online) SPL in the rotor disk plane for the rotor APC 11 × 4.7 SF at (a) 3000 and (b) 5000 rpm. Rotor blowing in the (solid black lines) upward direction, and (dashed red lines) downward direction.

First, differences can be observed for the tonal noise corresponding to the rpm. Indeed, differences of 2.0 and 5.7 dB are noted for 3000 rpm at 50 Hz and for 5000 rpm at 83.3 Hz, respectively. This tonal noise is due at least partially to the default of symmetry of the two-bladed rotor and differences expected between the two different setups.

Moreover, the broadband noise in the frequency range 100–800 Hz is higher when the flow is going in the downward direction, interacting with the test stand; differences up to 15 dB can be observed as compared to the case where the flow is going in the upward direction.

Except for those two differences, the results for the main tonal noise due to the BPF and for the broadband noise due to trailing edge noise are very similar between the two experimental configurations. In the remainder of the paper, all the rotors will be studied blowing in the upward direction (i.e., away from the test stand).

C. Motor noise

To assess whether the motor noise is of the same order of magnitude as the rotor noise, as put into evidence in Zawodny *et al.* (2016), a comparison of the spectra of the background noise (denoted "BGN"), the isolated motor noise, and the noise of the rotor ISAE 2 mounted on the motor is given in Figs. 8(a) and 8(b) at 40° for two different rpm. It can be seen that the noise coming from the isolated motor increases with the rpm with some tonal components

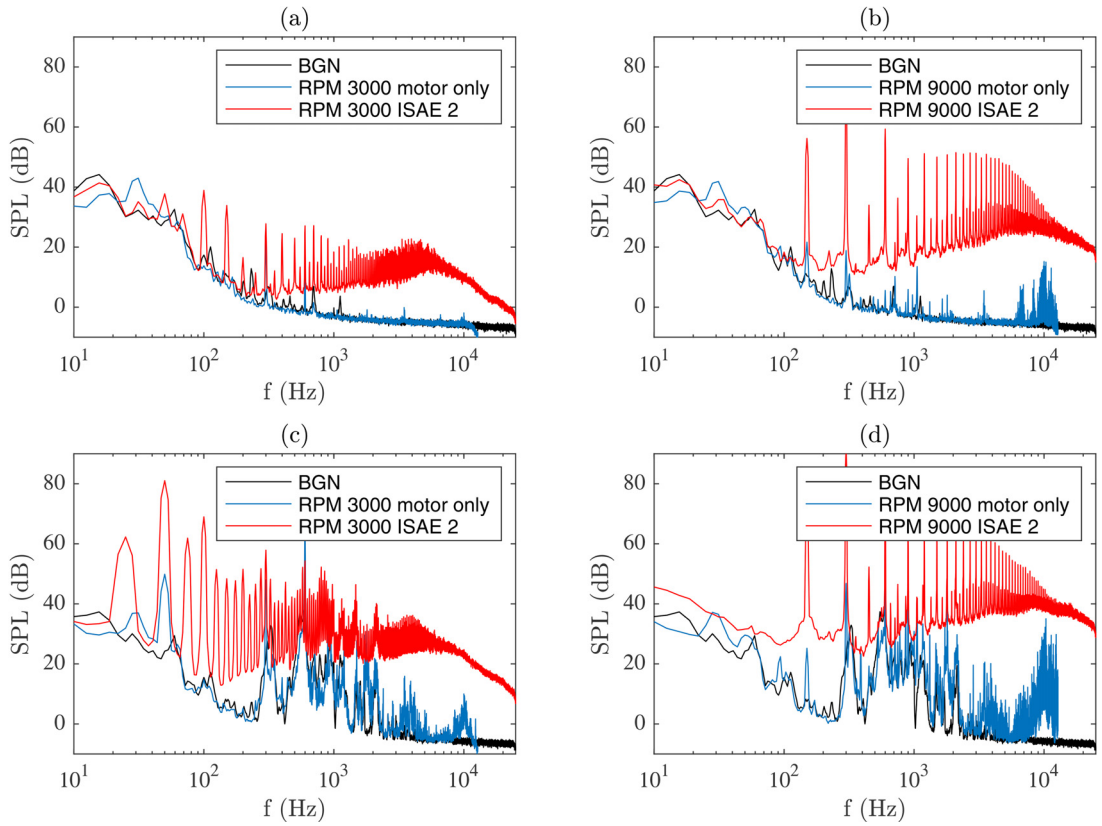

FIG. 8. (Color online) Background noise (BGN), unloaded motor, and ISAE 2 SPL at 40° [(a) and (b)] and at the near-field microphone [(c) and (d)] at 3000 [(a) and (c)] and 9000 [(b) and (d)] rpm.

https://doi.org/10.1121/10.0005068

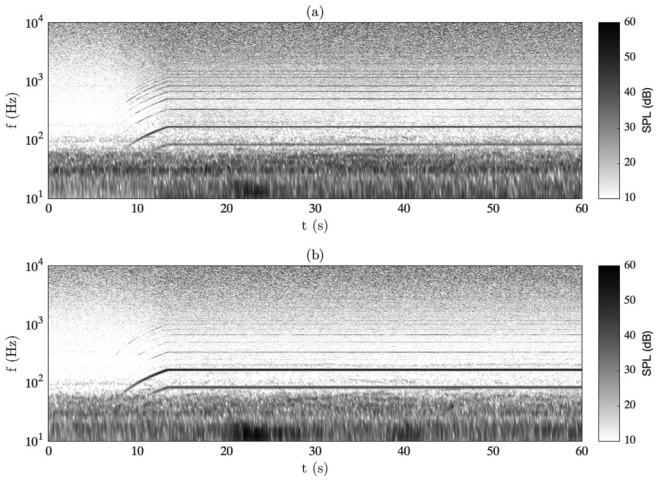

FIG. 9. Acoustic spectrogram of the rotor APC 9 × 6 SF (a) 60° above the rotor disk plane and (b) in the rotor disk plane.

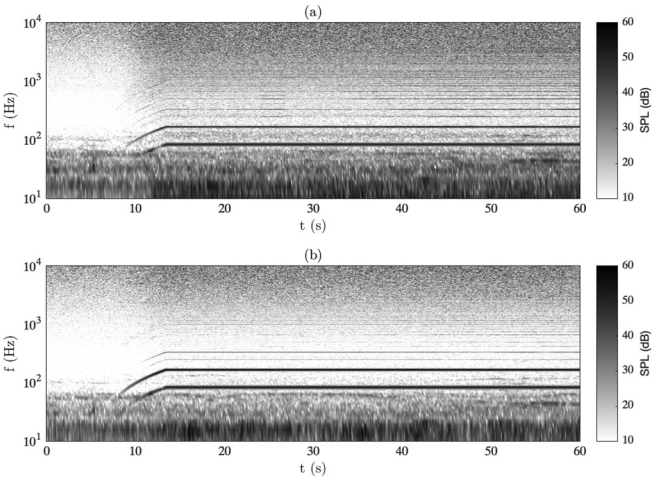

FIG. 10. Acoustic spectrogram of the rotor APC 11 × 4.7 SF (a) 60° above the rotor disk plane and (b) in the rotor disk plane.

in the frequency range 100–10 000 Hz and especially around 10 000 Hz for highest rpm. Moreover, the ISAE 2 rotor noise remains several dB higher than the isolated motor noise.

Figures 8(c) and 8(d) show that the isolated motor noise is strongest in the near field of the motor. In that case, the near-field rotor broadband noise seems affected by motor noise in the frequency range 300–2000 Hz, and one or two tones coming from the motor can be visible on rotor spectra at lowest rpm.

The motor used in this study thus seems to be silent enough to unambiguously extract rotor noise components at the far field. However, it should be pointed out that the noise coming from the motor might be different depending on whether the rotor is loaded or not.

D. Flow recirculation

Recently, Stephenson *et al.* (2019) and Nardari *et al.* (2019) observed that flow recirculation in closed anechoic rooms can result in a significant increase in higher harmonic noise. In Stephenson *et al.* (2019), an increase of more than 15 dB in some harmonics was observed for a 0.24 m diameter rotor in an anechoic room with wedge-tip to wedge-tip dimensions $3.65 \times 2.56 \times 3.26$ m^3. The diameters of the

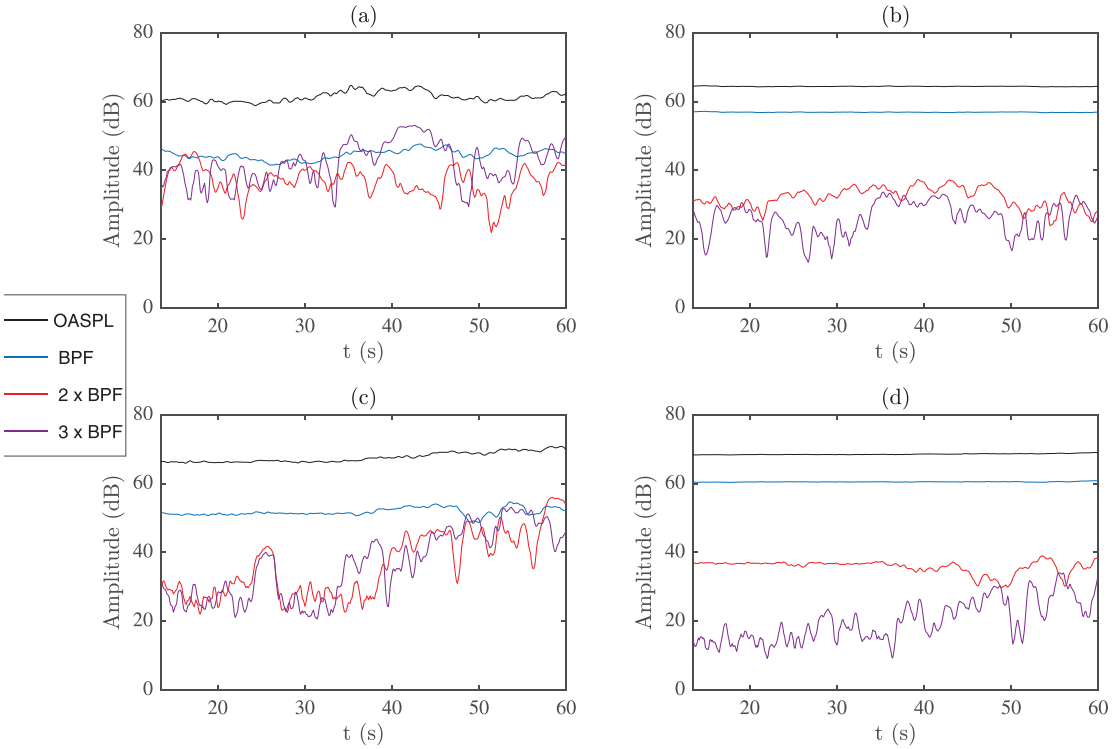

FIG. 11. (Color online) Evolution of the OASPL and main tones of the rotors APC 9 × 6 SF [(a) and (b)] and APC 11 × 4.7 SF [(c) and (d)]: 60° above the rotor disk plane [(a) and (c)] and in the rotor disk plane [(b) and (d)].

TABLE IV. Characteristics of the three printed ISAE 2 rotors.

Rotor	Printing inclination	Resin
ISAE 21	Inclination 1	Glass reinforced "Rigid" resin
ISAE 22	Inclination 2	Glass reinforced "Rigid" resin
ISAE 23	Inclination 1	"Grey Pro" resin

rotors used in the present study are within similar ranges, but the anechoic room is larger than that of Stephenson *et al.* (2019).

To check whether flow recirculation in our anechoic room influences the acoustic emissions of the rotors, a spectrogram of 60 s length with a sampling frequency equal to 0.1 s is plotted in Fig. 9 for the APC 9×6 SF rotor and in Fig. 10 for the APC 11×4.7 SF rotor. The rotor is rotated at rotational speeds from 0 to 5000 rpm and reaches its maximum speed at $t = 13.5$ s. For the APC 9×6 SF rotor, the spectrogram seems constant from $t = 13.5$ s to $t = 60$ s at both angles (i.e., in the rotor disk plane and 60° above the rotor disk plane). However, for the APC 11×4.7 SF rotor, an increase in the harmonics of the BPF can be observed, which suggests that, for this rotor, a flow recirculation in the anechoic room influences its acoustic emissions.

To provide a more quantitative analysis of the effects of the flow recirculation on the different acoustic characteristics of the rotor, the overall sound pressure levels (OASPLs) and the levels of the BPF and of its two first harmonics are monitored along time. The results are plotted in Fig. 11. The BPF considered here is $f_0 = 166$ Hz, corresponding to the maximum rotational speed of 5000 rpm. Thus, the results obtained before the rotor reaches its maximum speed at $t = 13.5$ s are not considered.

For the APC 9×6 SF rotor, in Figs. 11(a) and 11(b), the amplitudes of the four acoustic components vary in time but around a mean value that remains constant. Thus, for this rotor, as already expected from the spectrogram, there seem to be no effects of the flow recirculation on the acoustic emissions.

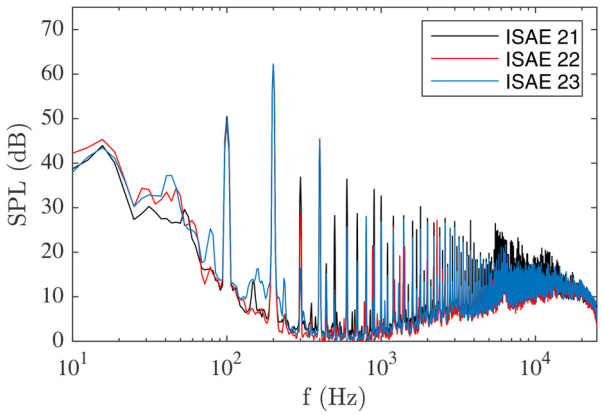

FIG. 12. (Color online) SPL of the three ISAE two-bladed rotors at 6000 rpm in the rotor disk plane.

For the APC 11×4.7 SF rotor, in Figs. 11(c) and 11(d), we can observe an increase in most of the amplitudes monitored in time. First, in the 60° plane, an increase of about 4 and 1 dB, respectively, is observed for the OASPL and the BPF between $t = 13.5$ and $t = 60$ s, whereas an increase of about 20 dB is noticed for the two first BPF harmonics. In the rotor plane, OASPL, BPF, and BPF first harmonic are almost constant, whereas the BPF second harmonic increases by about 10 dB.

In conclusion, for the APC 9×6 SF rotor, no noticeable effects of flow recirculation in the anechoic room are observed for both angles, whereas for the APC 11×4.7 SF rotor, a flow recirculation leading to an increase in some harmonics of the BPF is observed. Our experimental campaign thus permits us to accurately measure the acoustic emissions of similar rotors in hovering flight outdoors only up to a certain thrust value. Indeed, as a first approximation, the recirculation amplitude can be related to the induced velocity at the rotor disk plane, hence rotor thrust. For the APC 9×6 SF and APC 11×4.7 SF rotors, at 5000 rpm, thrust values are $T = 3.73$ N and $T = 6.32$ N, respectively. That is, our experimental campaign allows accurate measurements of rotor acoustic emissions in hovering flight outdoors at least up to 3.73 N.

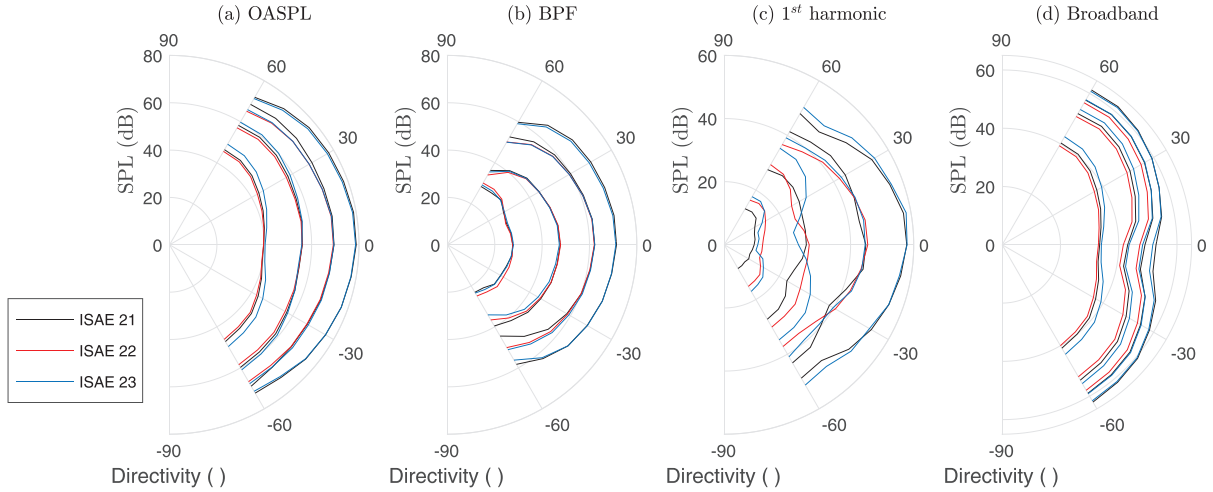

FIG. 13. (Color online) Directivity of the OASPL (a), the BPF (b), its first harmonic (c), and the broadband noise (d) of the three ISAE two-bladed rotors for [2000:2000:8000] rpm.

https://doi.org/10.1121/10.0005068

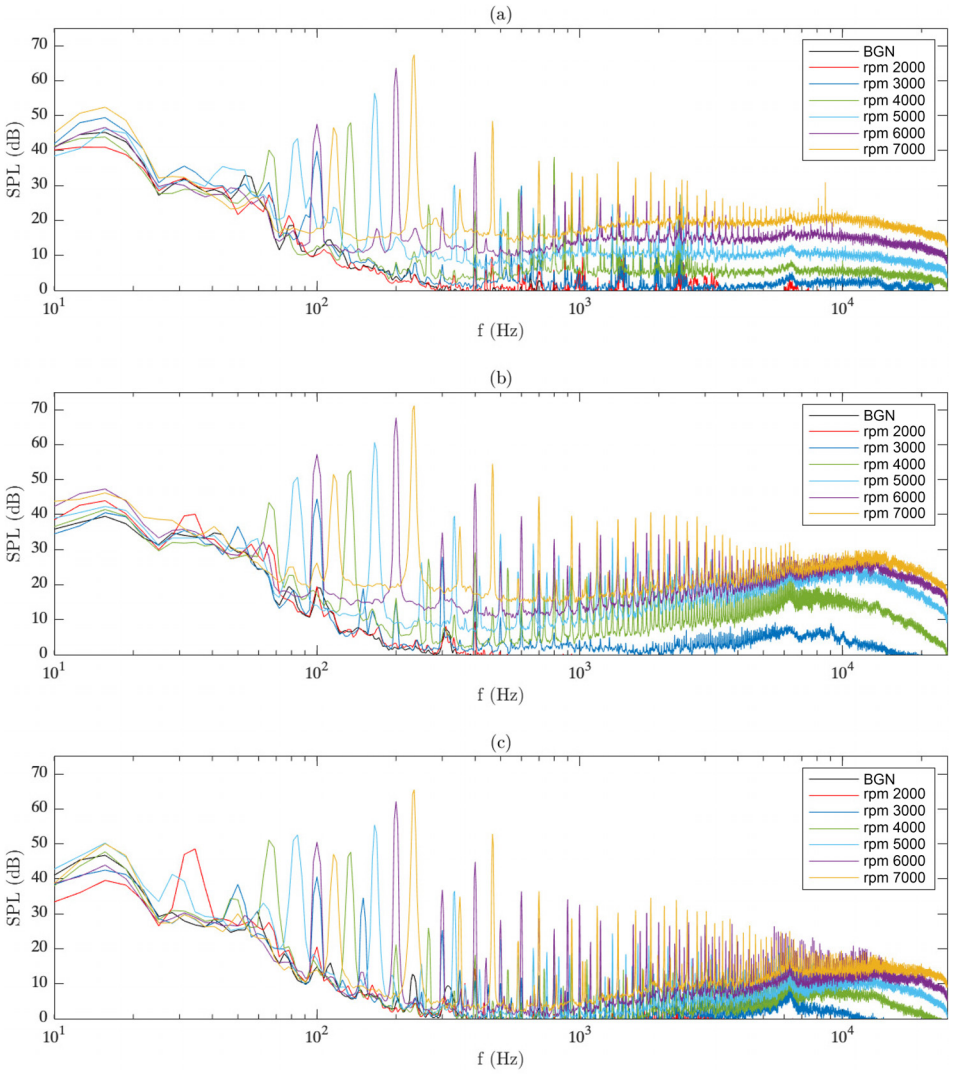

FIG. 14. (Color online) SPL of (a) APC 9×6 SF, (b) APC 11×4.7 SF, and (c) ISAE 2 rotors in the rotor disk plane.

E. 3D printing strategy

The stereolithography 3D printing was performed using a Form 2 printer from *formlabs*, and two photopolymer resins were tested: the standard Grey Pro gray resin and the glass reinforced Rigid white resin. To validate the 3D printing strategy, the assessment of the reproductibility from one rotor to another needs to be performed.

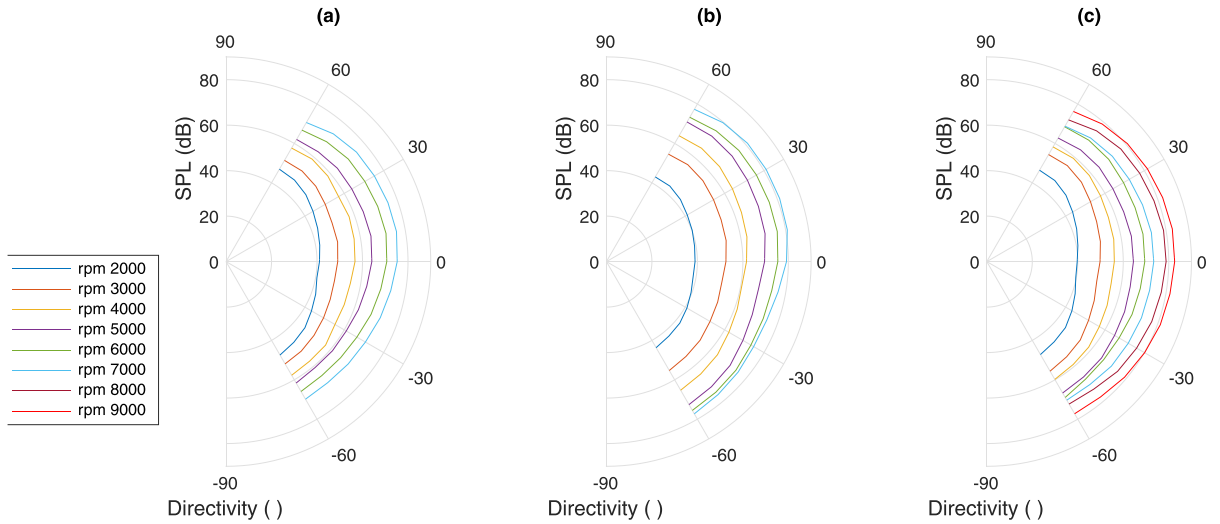

FIG. 15. (Color online) Directivity of the OASPL of the two-bladed rotors (a) APC 9×6 SF, (b) APC 11×4.7 SF, and (c) ISAE 2.

For this purpose, three two-bladed ISAE 2 rotors have been 3D-printed, namely ISAE 21, ISAE 22, and ISAE 23. Two rotors are printed with the same setup, changing the resin, and a third one is printed with a different printing direction, which may affect the rugosity direction at the surface. Rotor characteristics are presented in Table IV.

To qualitatively check the differences, the spectra at 6000 rpm in the rotor disk plane are plotted for the three rotors in Fig. 12.

It can be observed that the spectra are very similar. We note that a broadband noise centered around 6400 Hz can be seen. This small amplitude broadband noise is visible in the rotor disk plane for all the rotors tested and all the rpm. This noise component seems thus not related to the rotor noise and will not be considered in the rest of the paper. We suspect this noise component to be related to loaded motor noise. This will be investigated in the near future.

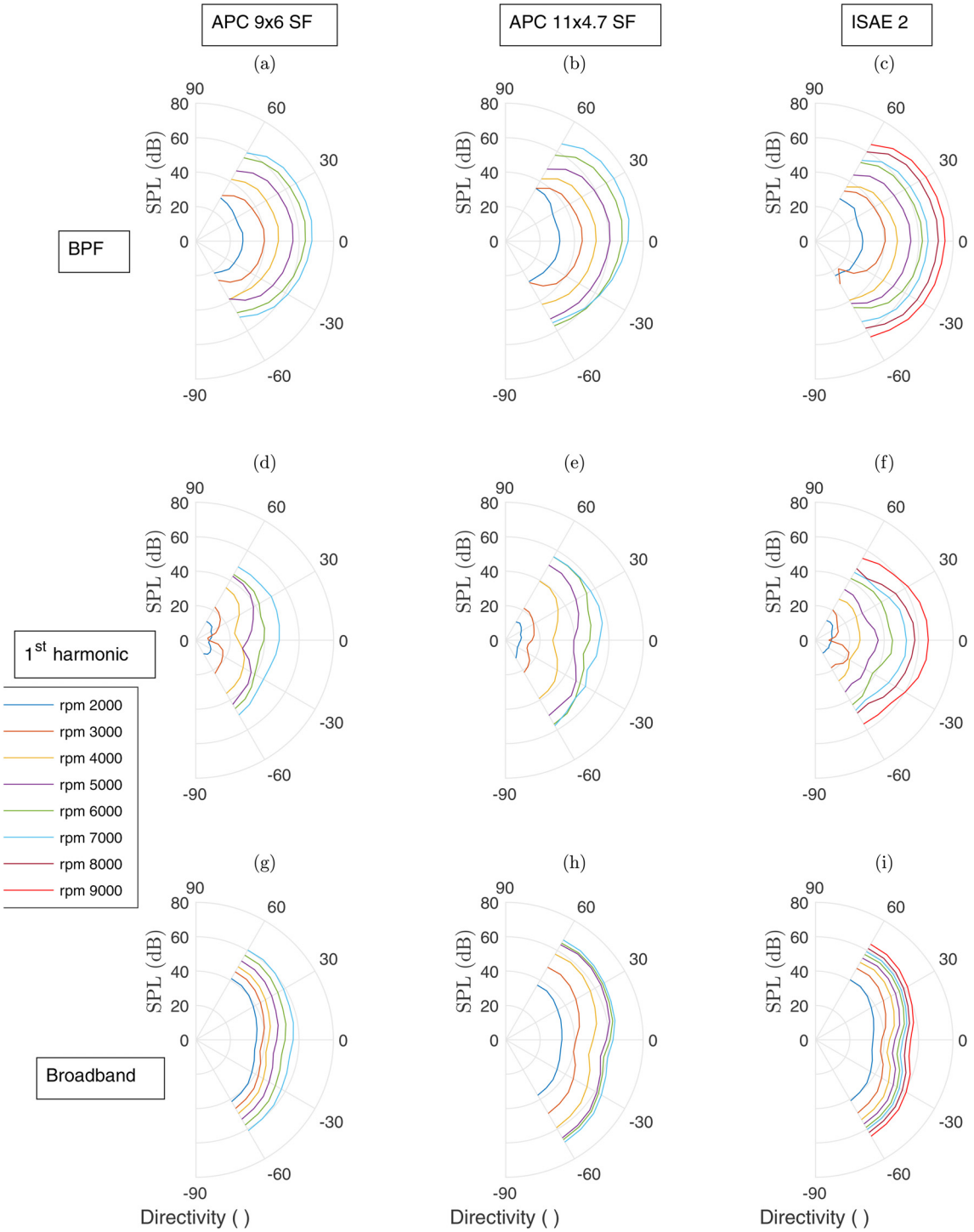

FIG. 16. (Color online) Directivity of the BPF [(a), (b), and (c)], of its first harmonic [(d), (e), and (f)], and of the broadband noise [(g), (h), and (i)] of the two-bladed rotors [(a), (d), and (g)] APC 9 × 6 SF, [(b), (e), and (h)] APC 11 × 4.7 SF, and [(c), (f), and (i)] ISAE 2.

https://doi.org/10.1121/10.0005068

To compare those spectra in a more quantitative way, several characteristics are studied as functions of the directivity angle in Fig. 13: the OASPL, the amplitude of the BPF and of its first harmonics, and the broadband trailing edge noise. The OASPL is computed by taking the integrated value of the autopower signal over the frequency range 80 Hz $<$ f $<$ 16 000 Hz. For the broadband noise, peaks are cleaned from the autopower before computing the integrated value over the frequency range 1000 Hz $<$ f $<$ 16 000 Hz. The two ranges are chosen up to the anechoicity limit of the room. Directivity plots are presented for [2000:2000:8000] rpm. Please note that for ISAE 22, the ramp in rpm was stopped at 6000 rpm as vibrations of the test stand were observed with the three-axis accelerometer.

For the OASPL, in Fig. 13(a), the difference is below 0.6 dB in the rotor disk plane for all rpm. Greater differences can be observed when increasing the directivity angle with differences up to 3.5 dB at $\pm 60^\circ$ for 2000 rpm. Overall, the higher the rpm, the lower the differences between the rotors. The same observation can be made for the amplitude of the BPF in Fig. 13(b) with differences up to 0.5 dB in the rotor disk plane and up to 6.5 dB at -60° for 6000 rpm. For the first harmonic of the BPF in Fig. 13(c), differences up to 8 dB can be observed for cases at 2000 and 4000 rpm. For the two highest rpm, the differences are below 1 dB in the rotor disk plane and below 6 dB everywhere else. Finally, for the broadband noise, in Fig. 13(d), the same pattern is recovered for all the rotors with differences below 3.5 dB everywhere. In conclusion, the 3D printing strategy is validated, and the glass reinforced Rigid white resin will be used in this study, as it limits rotor deformation due to inertial and aerodynamic forces.

IV. TWO-BLADED ROTOR AEROACOUSTICS

First, we will investigate the three two-bladed rotors considered in this study: APC 9 × 6 SF, APC 11 × 4.7 SF, and ISAE 2. Their acoustic spectra in the rotor disk plane are given in Fig. 14 for rotational speeds from 2000 to 7000 rpm. Please note the background noise is also given for comparison purposes. For all rpm, the main tone always corresponds to the BPF. Then tones are also visible at the harmonics of the BPF and at half of the BPF. Finally, for the three rotors, the amplitudes of all the tones and of the high-frequency broadband noise increase with the rpm, as expected.

When looking at the directivity, several characteristics of the spectra can be followed. First, the OASPL computed over a frequency range of 80 Hz $<$ f $<$ 16 000 Hz is plotted in Fig. 15. As expected, the amplitude of the OASPL increases with the rpm for all angles. At low rpm, the OASPL values are minimum at an angle of $\theta = -10^\circ$ and maximum at $\theta = \pm 60^\circ$. For example, for a rotational speed of 3000 rpm, minimum values of 48.4, 51.5, and 49.1 dB are obtained at an angle of $\theta = -10^\circ$, whereas maximum values of 51.9, 55.3, and 55.6 dB are obtained at $\theta = -60^\circ$ for APC 9 × 6 SF, APC 11 × 4.7 SF, and ISAE 2, respectively. This trend is visible up to a rotational speed of 4000 rpm. For higher rpm, the directivity of the OASPL changes with maximum values at $\theta = 10^\circ$ and minimum values at $\pm 60^\circ$.

The directivity of the amplitude of the BPF is plotted in Figs. 16(a)–16(c). The maximum values are located at $\theta = 10^\circ$ or $\theta = 20^\circ$, and the minimum value is always located at $\theta = -60^\circ$ for the three two-bladed rotors and for all rpm. This behavior is in agreement with the results of Zawodny *et al.* (2016), where the same directivity pattern is

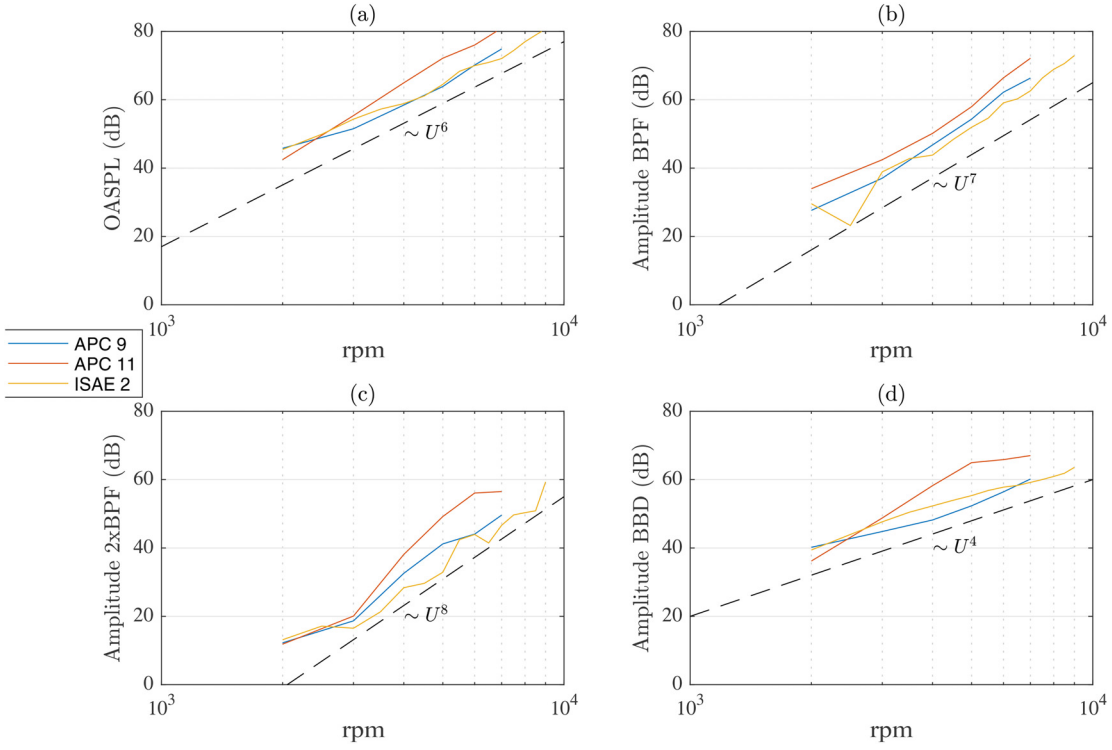

FIG. 17. (Color online) The scaling at 40° of the OASPL (a), the BPF (b), its first harmonic (c), and the broadband noise (d) as functions of the rpm.

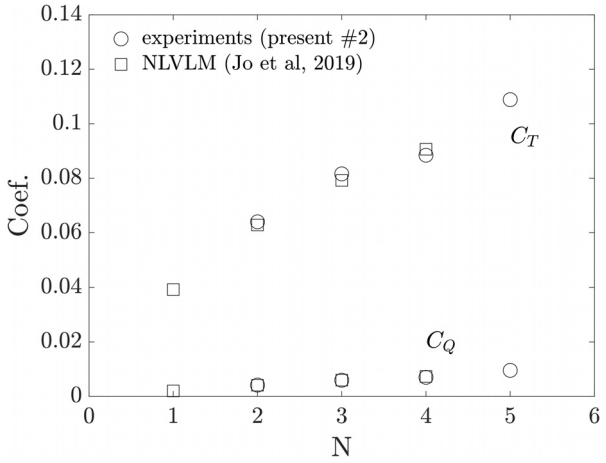

FIG. 18. Time-averaged thrust C_T and torque C_Q coefficients as a function of the number of blades N, obtained for ISAE rotors (NACA0012 blade sections, constant 10° pitch, constant chord). Data obtained by (Jo *et al.*, 2019) using low-order numerical simulations (NL-VLM) are added for the sake of comparison.

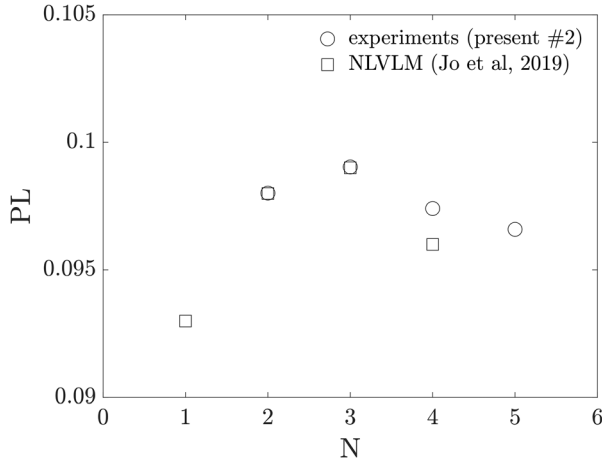

FIG. 19. Time-averaged power loading (PL) as a function of the number of blades N, obtained for ISAE rotors (NACA0012 blade sections, constant 10° pitch, constant chord). Data obtained by Jo *et al.* (2019) using low-order numerical simulations (NL-VLM) are added for the sake of comparison.

found for a DJI 9443 rotor and the same APC 11 × 4.7 SF. The directivity of the first harmonic of the BPF is plotted in Figs. 16(d)–16(f). For the two APC rotors, a minimum value can be found at $\theta \sim -10°$ for all rpm. For the ISAE 2 rotor, this behavior is only visible for rotational speeds lower than 4000 rpm. Then the directivity pattern changes, and a maximum value can be observed at $\theta = 10°$. The same change of behavior has been observed in Zawodny *et al.* (2016) for the directivity of the first harmonic of the BPF of a DJI 9443 rotor. The authors attributed this minimum value at $\theta \sim -10°$ to phase cancellation of thickness and loading noise sources. The directivity of the broadband noise computed over a frequency range of 1000 Hz < f < 16 000 Hz is plotted in Figs. 16(g)–16(i). For this noise component, a dipole-like pattern is obtained with a minimum value at $\theta = -10°$, i.e., aligned with the trailing edge and thus indicating the generation of trailing edge noise.

To conclude, empirical scaling laws are derived for the OASPL, the amplitude of the BPF and of its first harmonic, and the broadband noise, plotted as functions of the rpm in Fig. 17, for an angle of 40°. In Fig. 17(a), the OASPL is seen to increase globally with U^6 when increasing the rpm. In Figs. 17(b) and 17(c), the amplitudes of the BPF and of its first harmonic are observed to evolve with U^7 and U^8 when increasing the rpm, respectively. Finally, the broadband noise evolves with U^4. However, for the latter noise, one should remember that only the frequency range 1000 Hz < f < 16 000 Hz is considered. Moreover, it can be seen in Fig. 14 that the central frequency of the trailing edge noise increases with the rpm. Thus, the larger the rpm, the larger the part of the broadband noise that is out of the frequency range. Overall, differences on the order of magnitudes suggest that, in the absence of drastic changes of flow regimes, tonal noise will always dominate broadband noise at higher Reynolds numbers, which may not be the case at lower Reynolds numbers. Moreover, the fact that the amplitudes of the BPF and of its first harmonic in Figs. 17(b) and 17(c) constantly (i.e., over the whole range of rpm) scale with U^7

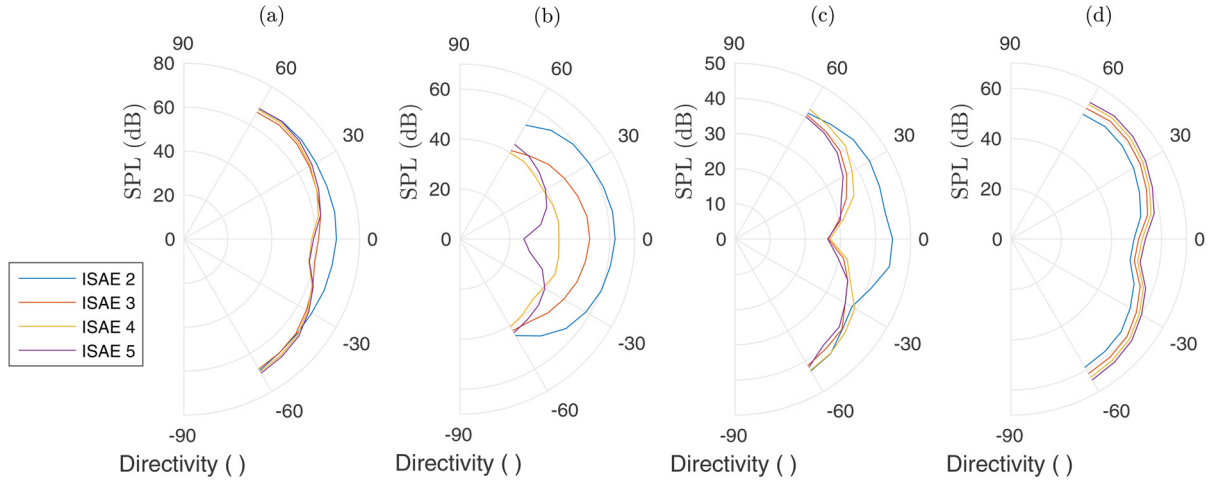

FIG. 20. (Color online) Directivity of the OASPL (a), the BPF (b), its first harmonic (c), and the broadband noise (d) at a target thrust of $T = 2.92$ N.

https://doi.org/10.1121/10.0005068

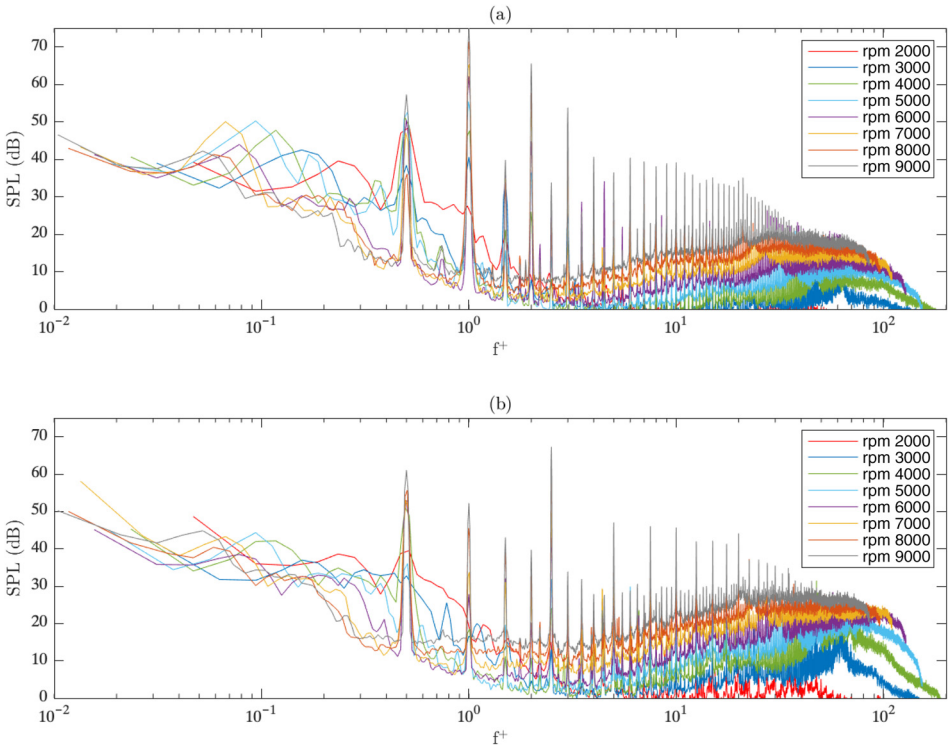

FIG. 21. (Color online) SPL for ISAE 2 (a) and ISAE 5 (b) rotors in the rotor disk plane.

and U^8, respectively, for the ISAE 2 and the APC 9×6 SF rotors suggests that the latter are not significantly affected by recirculation effects, even at high rotational speeds.

V. INFLUENCE OF THE NUMBER OF BLADES

The influence of the number of blades on the aerodynamics and aeroacoustics of low Reynolds number rotors is here investigated experimentally. Previous work by Jo *et al.* (2019) addressed a similar issue using a NL-VLM. The authors suggested that, for a given thrust, optimal aerodynamic efficiency is reached for a number of blades of 3 and that far-field noise monotonically decreases with the number of blades. Their results were obtained for constant chord and constant pitch rotors with NACA0012 blade sections, similar to the present ISAE 2 rotors. Here, we experimentally reproduce the numerical study by Jo *et al.* (2019).

Figure 18 shows the time-averaged thrust C_T and torque C_Q coefficients as functions of the number of blades N. The rpm for each value of N was determined in Jo *et al.* (2019) using NL-VLM to reach a target thrust of 2.92 N within 1%. The rpm were found to be 7600, 6000, 5300, and 4950 for $N = 1$, 2, 3, and 4, respectively. For $N = 5$, an rpm value of 4500 was found by extrapolating the experimental results, as it was not computed in Jo *et al.* (2019). Then experimental results were interpolated to found thrust and torque coefficients at rpm = 6000, 5300, 4950, and 4500 for N =2, 3, 4, and 5. The results showed that $T = 2.92$ N was achieved within 3.5%.

First it can be seen that both C_T and C_Q significantly increase with N, which is expected, since the rotor solidity

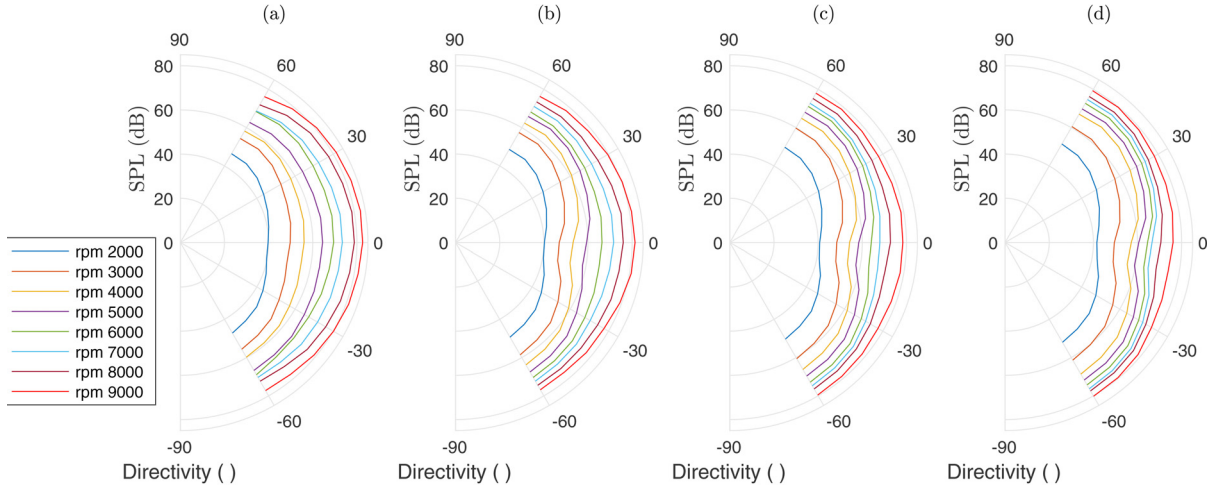

FIG. 22. (Color online) Directivity of the OASPL for ISAE 2 (a), ISAE 3 (b), ISAE 4 (c), and ISAE 5 (d) rotors in the rotor disk plane.

$\sigma = 2Nc/\pi D$ also increases. When scaling by σ is applied, the thrust-to-solidity ratio decreases with N (not shown here for the sake of conciseness), which most probably reflects the increasing influence of blade wake interactions. Second, it is shown that results obtained by Jo *et al.* (2019) using NL-VLM match within reasonable accuracy the present experimental data. Plotting the power loading $PL = T/2\pi fQ$ as a function of N in Fig. 19 shows that while C_T and C_Q increase monotonically with N, PL reaches a maximum for $N = 3$, corroborating previous results by Jo *et al.* (2019). However, it is worthy of mention that variations in PL remain small, within 3% for $N \in [2-5]$. In addition, we stress that increasing the number of blades will increase the overall rotor mass, which ultimately, from a practical perspective, should be taken into account when applying the thrust constraint.

Figure 20 shows directivity plots obtained for the four rotors at a target thrust of $T = 2.92$ N. Those directivity plots were found by extrapolating the experimental results. First, it can be seen from Fig. 20(a) that the integrated OASPL value decreases by about 10 dB in the rotor disk plane when increasing the number of blades. This is mainly due to the decrease in the BPF amplitude, as can be seen in Fig. 20(b). However, when increasing the number of blades, the broadband noise increases, as observed from Fig. 20(d). This counterbalances the decrease in the amplitude of the BPF and of its first harmonics and leads to an almost constant OASPL value at $\pm 60°$ for all the rotors. This direction

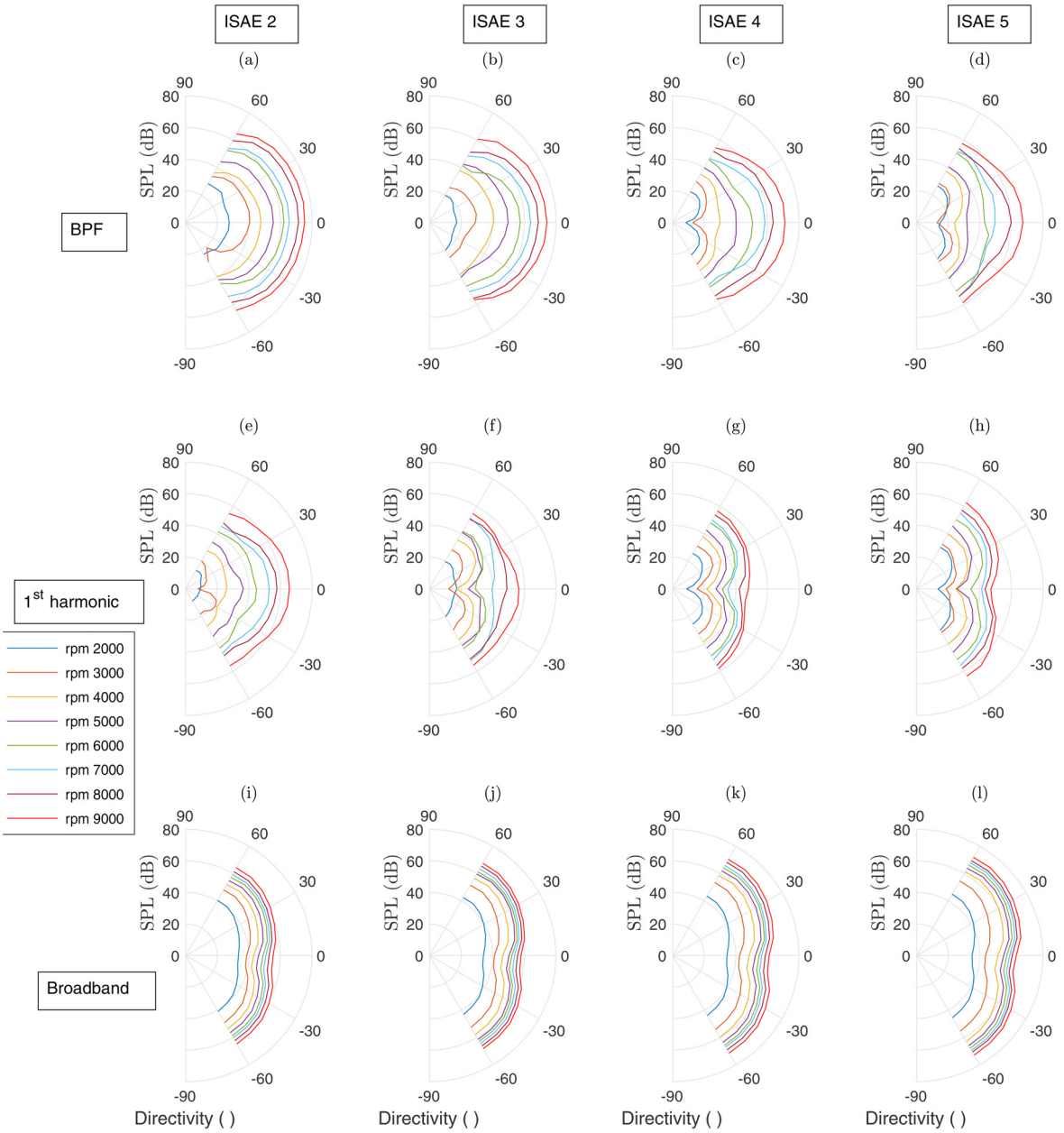

FIG. 23. (Color online) Directivity of the BPF [(a)–(d)], of its first harmonic [(e)–(h)], and of the broadband noise [(i)–(l)] for ISAE 2 [(a), (e), and (i)], ISAE 3 [(b), (f), and (j)], ISAE 4 [(c), (g), and (k)], and ISAE 5 [(d), (h), and (l)] rotors in the rotor disk plane.

https://doi.org/10.1121/10.0005068

corresponds notably to the direction of the ground when the UAV is flying, reducing the interest of increasing the number of blades of the rotor.

To further analyse the influence of N on rotor aeroacoustics, we look at the acoustic spectra and directivity for different values of rpm. First, the acoustic spectra in the rotor disk plane for ISAE 2 and ISAE 5 rotors are shown in Fig. 21. Note that the dimensionless frequency $f^+ = f/BPF$ is used in abscissa to facilitate comparison between all cases. The tone of highest amplitude always corresponds to the BPF. Then tones are also visible at the harmonics of the BPF and at half of the BPF. Finally, for all rotors (only two- and five-bladed rotors are shown for purposes of clarity), the amplitudes of all the tones and of the high-frequency broadband noise increase with the rpm, as previously observed for the two-bladed rotors.

When comparing the different rotors, a decrease in BPF tonal noise with the increase in number of blades is observed at iso-rpm. This effect most probably arises from an increase in thrust with N, which causes an increase in induced velocity and hence a decrease in blade effective angle of attack, which in turn decreases the loading of each blade. This decrease in blade loading is further enhanced by blade wake interactions, as evidenced from Fig. 18, where it can be observed that C_T is not a linear function of N; $C_T(N) \neq N \times C_T(N=1)$ under iso-thrust constraint. Then an increase in the broadband noise is observed. Those two observations corroborate previous numerical results by Jo *et al.* (2019). Finally, an increase in broadband noise in the frequency range 100 Hz $<$ f $<$ 1000 Hz with the number of blades is highlighted. This trend is most likely due to increased blade wake interactions, as observed in Brooks and Burley (2001).

The OASPL, computed over a frequency range of 80 Hz $<$ f $<$ 16 000 Hz is plotted in Fig. 22. As expected, the amplitude of the OASPL increases with the rpm for all angles. Moreover, for all the rotors, a minimum value can be found at $\theta \sim -10°$ for low rpm. Then, when increasing the rpm, the directivity pattern changes, and a maximum value can be observed at $\theta = 10°$. This change of behavior, already observed for the two-bladed rotors in Sec. IV, is due to the change of the directivity pattern of the amplitude of the BPF and of its first harmonic.

The directivity of the amplitude of the BPF is plotted in Figs. 23(a)–23(d). For the two- and three-bladed rotors, the maximum values are located at $\theta = 10°$ or $\theta = 20°$, and the minimum value is always located at $\theta = -60°$ for all rpm. However, for the rotors with four and five blades, a minimum value can be found at $\theta \sim -10°$ for low rpm, and a maximum value can be observed at $\theta = 10°$ for high rpm. The directivity of the first harmonic of the BPF is plotted in Figs. 23(e)–23(h). For the two- and three-bladed rotors, a minimum value can be found at $\theta \sim -10°$ for low rpm, and a maximum value can be observed at $\theta = 10°$ for high rpm. Moreover, for the rotors with four and five blades, a minimum value can be found at $\theta \sim -10°$ for all rpm. The directivity of the broadband noise computed over a frequency range of 1000 Hz $<$ f $<$ 16 000 Hz is plotted in Figs. 23(i)–23(l). For this noise component, a dipole-like pattern is obtained with a minimum value at $\theta = -10°$, as expected for trailing edge noise.

To conclude, scaling laws are derived for the OASPL, the amplitude of the BPF and of its first harmonic, and the

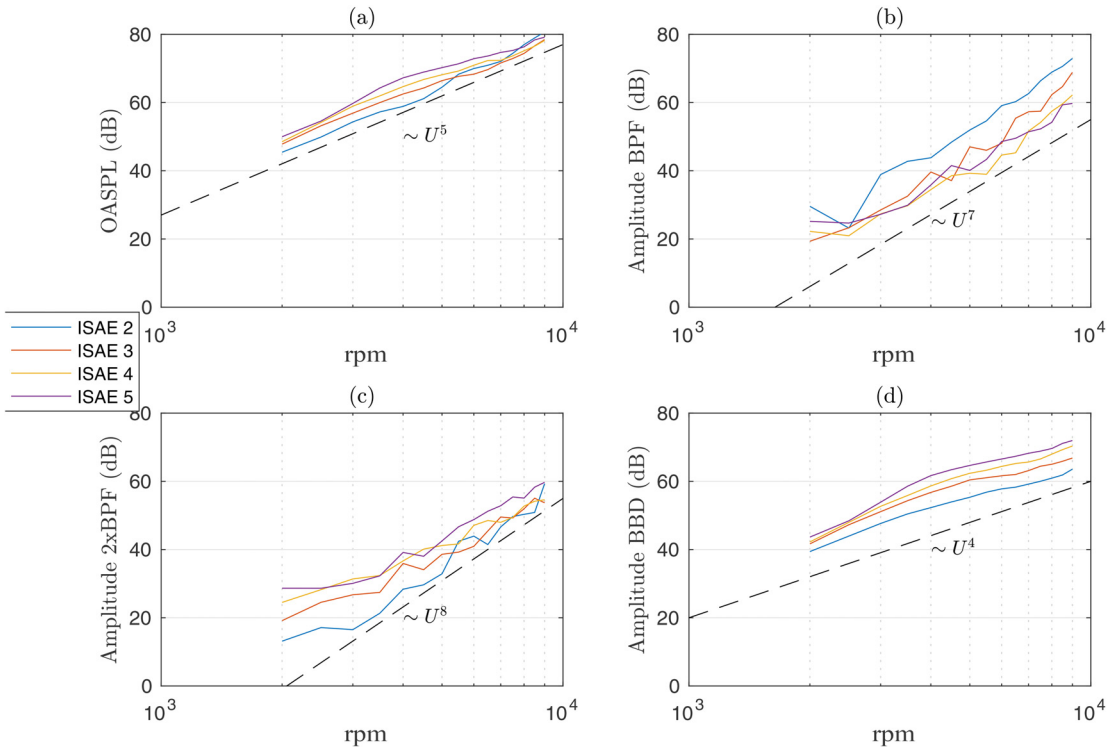

FIG. 24. (Color online) The scaling at 40° of the OASPL (a), the BPF (b), its first harmonic (c), and the broadband noise (d) as functions of the rpm.

broadband noise, plotted as functions of the rpm in Fig. 24. The overall trends are very similar to those previously found for two-bladed rotors. However, additional configurations with different chord and twist laws and different blade profiles should be investigated to assess the universality of these scaling laws. Finally, the fact that the amplitudes of the BPF and of its first harmonic in Figs. 24(b) and 24(c) constantly (i.e., over the whole range of rpm) scale with U^7 and U^8 for all the rotors suggest that we are not too much affected by recirculation effects, even at high rotational speeds.

VI. CONCLUSION

In this paper, an experimental characterisation of low Reynolds number rotors is performed in an anechoic room.

Two commercially available two-bladed APC 9×6 SF and APC 11×4.7 SF rotors, as well as four 3D-printed rotors with different numbers of blades (from two to five) are tested. The latter have an NACA0012 blade section profile, extruded in the radial direction with constant chord and constant 10° pitch.

The experimental setup is validated using comparison with existing data from the literature. The unloaded motor noise is compared to the rotor noise. The effects of possible flow recirculation in the anechoic room, of the blowing direction, and of the 3D printing strategy are analysed. It is concluded that the experimental setup is well suited for the thorough investigation of rotor noise and may serve as a benchmark for the validation of numerical approaches. All the results will be available as an open database for the UAV acoustic community to help in drawing general guidelines for the design of low noise rotors.

For all the rotors studied, in the far-field spectra, a dominant tonal frequency at the BPF together with its harmonics and with a broadband trailing edge noise are observed. The directivities of the OASPL, of the amplitude of the BPF and of its first harmonics, and of the high-frequency broadband noise are then analysed. An increase in those four noise sources is observed with rotational speed (rpm), for all angular positions of the observer. More precisely, an interesting change of pattern is observed for the amplitudes of the BPF and of its first harmonic, with a minimum value at $\theta \sim -10°$ for low rpm and/or high number of blades and a maximum value at $\theta \sim 10°$ for high rpm and/or low number of blades. This change in directivity leads to a similar change of directivity of the OASPL. The same change of behavior has been observed in the literature and was attributed to phase cancellation of thickness and loading noise sources. Finally, for the directivity of the broadband noise, a dipole-like pattern is obtained with a minimum value at $\theta = -10°$, as expected for trailing edge noise.

Also, iso-thrust conditions are analysed between the four 3D-printed rotors with different numbers of blades (from two to five). In a previous work, using a NL-VLM, optimal aerodynamic efficiency was reached for a number of blades of 3 for a given thrust of $T = 2.92$ N. In the present study, we recover the thrust and torque values of the NL-VLM calculation with reasonable accuracy and corroborate numerical results in that optimal aerodynamic efficiency is obtained with three blades. The spectrum characteristics at a target thrust of $T = 2.92$ N are then investigated. For the integrated OASPL value, a decrease in about 10 dB is observed in the rotor disk plane when increasing the number of blades. This is mainly due to the decrease in the BPF amplitude with the number of blades. However, when increasing the number of blades, the broadband noise increases, counterbalancing the decrease in the amplitude of the BPF and of its first harmonics and leading to an almost constant OASPL value at $\pm 60°$ for all the rotors.

ACKNOWLEDGMENTS

The authors gratefully acknowledge financial support from the Direction Générale de l'Armement (DGA). They are also grateful to the entire Institut Supérieur de l'Aéronautique et de l'Espace (ISAE-SUPAERO) technical team for the success of this test campaign.

APC (**2021**). "APC model aircraft propellers," Landing Products, Inc. (Woodland, CA), www.apcprop.com (Last viewed 1/8/2020).

Bendat, J., and Piersol, A. (**2010**). in *Random Data: Analysis and Measurement Procedures*, 4th ed. (Wiley, New York), Chap. 9.

Brandt, J., Deters, R., Ananda, G., Dantsker, O. D., and Selig, M. S. (**2020**). "UIUC Propeller Data Site," University of Illinois at Urbana-Champaign, http://m-selig.ae.illinois.edu/props/propDB.html (Last viewed 1/8/2020).

Brentner, K., and Farassat, F. (**1994**). "Helicopter noise prediction: The current status and future direction," J. Sound Vib. **170**(1), 79–96.

Brooks, T., and Burley, C. (**2001**). "Rotor broadband noise prediction with comparison to model data," in *Proceedings of the 7th AIAA/CEAS Aeroacoustics Conference*, May 28–30, Maastricht, Netherlands, p. 2210.

Désert, T. (**2019**). "Étude aéropropulsive d'un micro-drone à voilure tournante pour l'exploration martienne" ("Aerodynamic design of a Martian micro air vehicle"), Ph.D. dissertation, ISAE-SUPAERO, Toulouse, France.

Désert, T., Jardin, T., Bézard, H., and Moschetta, J. (**2019**). "Numerical predictions of low Reynolds number compressible aerodynamics," Aerosp. Sci. Technol. **92**(1), 211–223.

Deters, R., Ananda Krishnan, G., and Selig, M. (**2014**). "Reynolds number effects on the performance of small-scale propellers," in *Proceedings of the 32nd AIAA Applied Aerodynamics Conference*, June 16–20, Atlanta, GA, p. 2151.

George, A. (**1978**). "Helicopter noise: State-of-the-art," J. Aircraft **15**(11), 707–715.

Intaratep, N., Alexander, W., Devenport, W., Grace, S., and Dropkin, A. (**2016**). "Experimental study of quadcopter acoustics and performance at static thrust conditions," in *Proceedings of the 22nd AIAA/CEAS Aeroacoustics Conference*, May 30–June 1, Lyon, France, p. 2873.

ISAE-SUPAERO (**2021**). "ISAE-SUPAERO Dataverse," https://dataverse.isae-supaero.fr, https://doi.org/10.34849/C73YB7 (Last viewed 1/5/2021).

Jo, Y., Jardin, T., Gojon, R., Jacob, M., and Moschetta, J. (**2019**). "Prediction of noise from low Reynolds number rotors with different number of blades using a non-linear vortex lattice method," in *Proceedings of the 25th AIAA/CEAS Aeroacoustics Conference*, May 20–23, Delft, Netherlands, p. 2615.

Nardari, C., Casalino, D., Polidoro, F., Coralic, V., Lew, P., and Brodie, J. (**2019**). "Numerical and experimental investigation of flow confinement effects on UAV rotor noise," in *Proceedings of the 25th AIAA/CEAS Aeroacoustics Conference*, May 20–23, Delft, Netherlands, p. 2497.

Serré, R., Fournier, H., and Moschetta, J. (**2019a**). "A design methodology for quiet and long endurance MAV rotors," Int. J. Micro Air Veh. **11**, 1–14.

Serré, R., Gourdain, N., Jardin, T., Jacob, M., and Moschetta, J. (**2019b**). "Towards silent micro-air vehicles: Optimization of a low Reynolds number rotor in hover," Int. J. Aeroacoust. **18**(8), 690–710.

https://doi.org/10.1121/10.0005068

Stephenson, J., Weitsman, D., and Zawodny, N. (**2019**). "Effects of flow recirculation on unmanned aircraft system (UAS) acoustic measurements in closed anechoic chambers," J. Acoust. Soc. Am. **145**(3), 1153–1155.

Tinney, C., and Sirohi, J. (**2018**). "Multirotor drone noise at static thrust," AIAA J. **56**(7), 2816–2826.

Yoon, S., Diaz, P., Boyd, D., Jr., Chan, W., and Theodore, C. (**2017**). "Computational aerodynamic modeling of small quadcopter vehicles," in *Proceedings of AHS 73rd Annual Forum*, May 9–11, Fort Worth, TX.

Zawodny, N., and Boyd, D., Jr. (**2017**). "Investigation of rotor-airframe interaction noise associated with small-scale rotary-wing unmanned aircraft systems," in *Proceedings of AHS 73rd Annual Forum*, May 9–11, Fort Worth, TX.

Zawodny, N., Boyd, D., Jr., and Burley, C. (**2016**). "Acoustic characterization and prediction of representative, small-scale rotary-wing unmanned aircraft system components," in *Proceedings of AHS 72nd Annual Forum*, May 16–19, West Palm Beach, FL.